Transaction B: Mechanical Engineering
Vol. 16, No. 1, pp. 40–52

SCIENTIA IRANICA

Effect of Reduced Frequency on the Aerodynamic Behavior of an Airfoil Oscillating in a Plunging Motion

M.R. Soltani[1,*] and F. Rasi Marzabadi[1]

Abstract. *A series of low speed wind tunnel tests were conducted to study the unsteady aerodynamic behavior of an airfoil sinusoidally oscillating in plunge. The experiments included measuring the surface pressure distribution over a range of reduced frequencies, $k = 0.03 - 0.06$. In addition, steady state data were acquired and were used to furnish a baseline for further analysis and comparison. The model was oscillated with amplitude of ± 15 cm and at three different mean angles of attack of 0°, 10° and 18°. The unsteady aerodynamic loads were calculated from the surface pressure measurements, 64 ports, along the chord for both upper and lower surfaces. The plunging displacements were transformed into the equivalent angle of attack. Variations of the pressure coefficients and aerodynamic loads with the equivalent angle of attack showed strong sensitivity to the reduced frequency and mean angles of attack.*

Keywords: *Plunging; Unsteady aerodynamics; Airfoil; Wind tunnel; Reduced frequency; Hysteresis loop.*

INTRODUCTION

Unsteady flows and dynamic stall prediction methods used by the industry are largely based on empirical or semi-empirical approaches that are fast and relatively accurate; where non-linear effects are not too great. Increased development in aircraft and wind turbine aerodynamics has created a demand for more detailed information of non-linear unsteady loads, the dynamic response and aero elastic stability caused by dynamic motions, including dynamic stall effects [1].

Wind turbine or helicopter rotor blade sections encounter large time dependent variations in angle of attack, as a result of control input angles, blade flapping, structural response and wake inflow. In addition, the blade sections encounter substantial periodic variations in local velocity and sweep angle. Thus, the unsteady aerodynamic behavior of the blade sections must be properly understood to enable accurate predictions of the air loads and aero elastic response of the rotor system [2].

One underlying assumption in most aerodynamic models is that the effects of all blade motions and wake inflow variations can be adequately represented by an equivalent angle of attack. However, some studies [3-5] have postulated that fundamental differences exist in the air loads when different modes of motion are imposed (i.e., pitching versus plunging displacements). Most angle of attack changes that the rotor blades encounter are, in fact, due to variations in the flapping and elastic bending of the blade, i.e., a plunging forcing type [6].

Virtually all of the available unsteady air load data are for pitching motions and information about the aerodynamic behavior of a model in a plunging motion is rare. This study addresses some of the most important aspects of the unsteady aerodynamic behavior of an airfoil oscillating in plunge at a subsonic regime. The experiments were conducted at a freestream velocity of 30 m/sec, corresponding to the Reynolds number of $0.42 * 10^6$, and at an oscillation amplitude of ± 15 cm. This investigation involves the effect of reduced frequency on the pressure, hence, aerodynamic, coefficients of the airfoil at low to moderate angles of attack. Note that in a plunging motion, the

1. *Department of Aerospace Engineering, Sharif University of Technology, P.O. Box 11155-8639, Tehran, Iran.*
*. *Corresponding author. E-mail: msoltani@sharif.edu*

Received 24 July 2006; received in revised form 17 September 2007; accepted 23 December 2007

model moves vertically up and down inside the tunnel test section, therefore, variations of the aerodynamic loads are caused by pure angle of attack changes, while they are functions of both angle of attack and pitching rate in a pitching motion.

EXPERIMENTAL APPARATUS

All experiments were conducted in a low speed wind tunnel in Iran. It is a closed circuit tunnel with a rectangular test section of $80 * 80 * 200$ cm^3. The test section speed varies continuously from 10 to 100 m/sec, corresponding to a Reynolds number of up to $5.26 * 10^6$ per meter. The inlet of the tunnel has a 7 : 1 contraction ratio with four, large anti-turbulence screens and a honeycomb in its settling chamber to reduce the tunnel turbulence level to less than 0.1 percent in the test section, as measured by the authors. Figure 1 shows the tunnel used for this study. The model considered in the present study has a 25 cm chord, an 80 cm span and is a section of a 660 kW wind turbine blade under construction. This model is equipped with 64 pressure orifices on its upper and lower surfaces. The pressure ports are located along the chord at an angle of 20 degrees with respect to the model span to minimize disturbances from the upstream taps (Figure 2). Data are obtained using sensitive pressure transducers. Due to the high number of pressure ports and the size of the selected pressure transducers, it was impossible to place the transducers inside the model. Therefore, extensive experiments were conducted to ensure that the frequency response of the pressure-measuring system was kept well above the highest frequency to be measured [7,8]. Finally, the tube length and material that gave a minimum time lag for all applied pressures were selected. For the selected tubes, the maximum amount of time lag was less than 0.01 sec., i.e., the frequency response at the end of

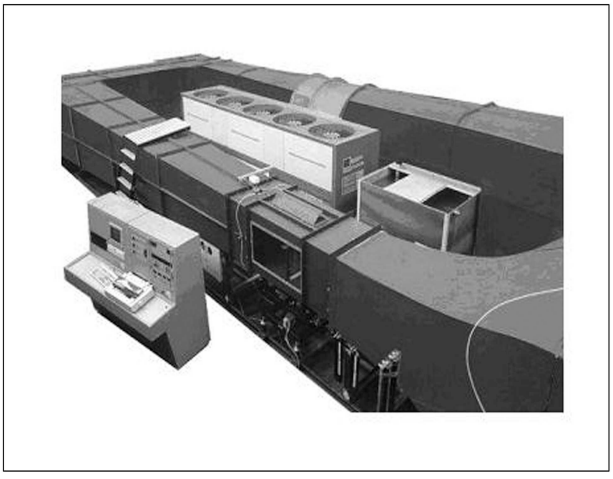

Figure 1. Low speed wind tunnel.

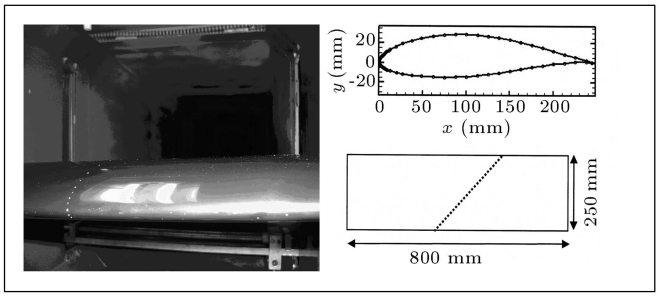

Figure 2. Airfoil model and the location of the pressure ports.

the tubes, including the transducer's volume, viscosity, and all other factors, was greater than 100 Hz. Each transducer data is collected via a terminal board and transformed to the computer through a 12-bit Analog-to-Digital (A/D) board capable of an acquisition rate of up to 500 kHz per channel.

The airfoil surface pressure distribution was measured at a Reynolds number of $0.42 * 10^6$ and over a range of reduced frequencies, $k = 0.03 - 0.06$, which are the effective reduced frequencies for this section of the aforementioned wind turbine blade under real operating conditions. The static angles of attack were varied from -5 to 23 degrees.

The plunging system for the present experiments incorporates a crankshaft to convert the circular motion of the motor to reciprocal motion, which is transferred to the model by means of rods. This system can oscillate the model with frequencies ranging from 1 to 4 Hz. Figure 3 shows the plunging mechanism used in this investigation (note that all equipment was designed and manufactured particularly for this experiment).

The dynamic oscillatory data presented here are an average of several cycles at a sample rate based on the oscillation frequency. Various data acquisition rates were examined to find the best combination, which would provide as many cycles of quality data as possible. Raw data were then digitally filtered using a low-pass filtering routine. During the filtering process, cut off and transition frequencies were varied until the deviation between the original and the filtered data was a minimum. Finally, all data were corrected for the solid tunnel sidewalls and the wake blockage effects using the method explained in [9]. Furthermore, an analytical approach was used to estimate the errors involved in the authors measurements [10]. The overall uncertainty obtained in the pressure coefficients was less than $\pm 3\%$ of the total C_P values.

RESULTS AND DISCUSSION

An extensive experimental investigation was conducted on an airfoil oscillating in plunge mode over a range of reduced frequencies, $k = 0.03 - 0.06$. The plunging

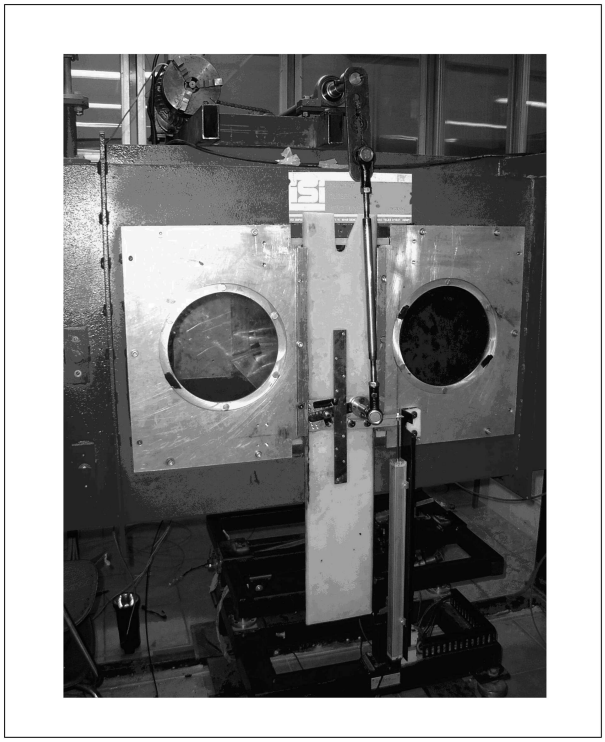

Figure 3. Plunging oscillation system.

displacements were transformed into the equivalent angle of attack using the potential flow transformation formula, $\overline{\alpha}_{\rm eq} = ik\overline{h}$, where $\overline{\alpha}_{\rm eq}$ is in radians and $\overline{h}$ has been nondimensionalized, with respect to the model semi-chord. The mean angle of attack was, of course, added to the equivalent angle [3,6].

From the above transformation formula, the effect of the plunging motion on the induced angle of attack is evident. As the plunging amplitude or the reduced frequency increases, the values of the induced angle of attack also increase. The airfoil plunges sinusoidal with time, hence, the corresponding induced angle of attack, which is due to the oscillation time history effects on the vertical motion of the model, is 90 degrees out of phase, with respect to the plunging motion. Figure 4 shows an example of the variation of the equivalent angle of attack for one oscillation cycle, with respect to its corresponding time history of the plunging motion. It can be seen that $\alpha_{\rm eq}$ is a maximum or minimum

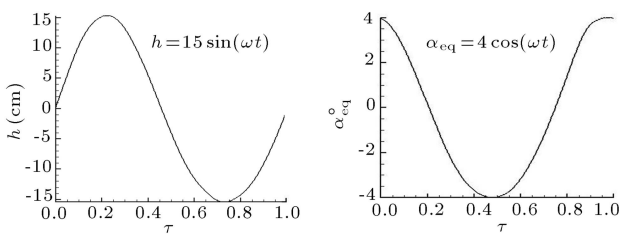

Figure 4. Time history of the plunging motion and its corresponding equivalent angle of attack.

whenever $h = 0$ during upstroke or down stroke, respectively.

Unsteady Pressure Coefficient Data

Figures 5 to 7 show variations of the pressure coefficient with the equivalent angle of attack for several pressure ports, both upper and lower surfaces, at three mean incident angles, $\alpha_0 = 0°$, $10°$ and $18°$. The model was oscillated at three different reduced frequencies, $k = 0.03$, 0.045 and 0.06, and at a constant plunging amplitude of ± 15 cm. The static data are also shown in each figure for comparison. The position of the pressure port under study is also shown on the top of each figure.

The data are shown for pressure ports located at $x/c = 2\%$, 15%, 30%, 50%, and 85%, for both upper and lower surfaces. In this way, one can compare pressure variations for ports located at the same x/c locations, but on the upper or lower surfaces of the model.

From Figure 5, it is seen that, as k increases, the corresponding equivalent angle of attack increases too, hence, the shape of the hysteresis loop varies. For the lowest reduced frequency case, $k = 0.03$, the hysteresis loops, for all upper surface pressure ports examined in Figure 5, form a "figure eight" shape. During increasing angles of attack, the dynamic data lags their corresponding static one. A similar trend happens in the downstroke portion of the motion, thus, there is variations on C_P that results in crossing over. Furthermore, this crossover point does not occur at the same angle of attack for all pressure ports, as seen from Figure 5. It varies from $\alpha = -1°$ for the $x/c = 2\%$ port to about $\alpha = 1°$ for the $x/c = 50\%$ pressure port. Similar phenomenon happens for the lower surface for $k = 0.03$ too (Figures 5a-5h). The formation of this "figure eight" shape is, maybe, due to the wake effect. The direction of the wake vortices is different in the upstroke and downstroke motions, which results in this lead-lag effect. Also, there are different distances between the wake vortices and location of the pressure ports, so the occurrence of the crossover point is not at the same angle of attack for all pressure ports. However, for the higher reduced frequency cases, $k = 0.045$ and 0.06, the direction of the loops is counterclockwise for all pressure ports located on the upper surface, from the leading edge to $x/c = 50\%$ (Figures 5a-5g). At the lower surface, the direction of the loops for all ports is clockwise for these two reduced frequencies (Figures 5b-5h). For these two higher reduced frequency cases, because of the higher oscillation velocity, the wake effects result in the aforementioned direction of the loops. Furthermore, Figure 5 shows that the C_P variation for the pressure port located at $x/c = 85\%$ of the model, does not vary significantly with angle of attack and C_P remains

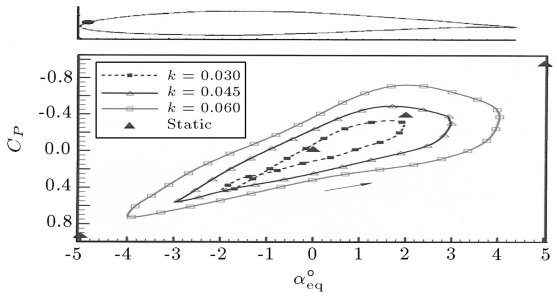

(a) $x/c = 2\%$ upper surface

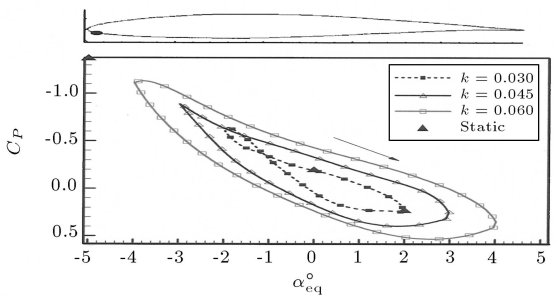

(b) $x/c = 2\%$ lower surface

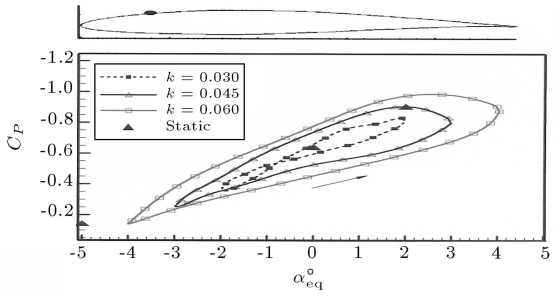

(c) $x/c = 15\%$ upper surface

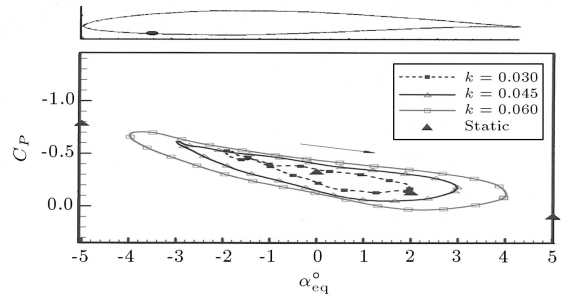

(d) $x/c = 15\%$ lower surface

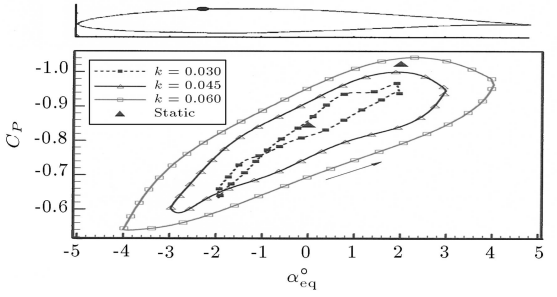

(e) $x/c = 30\%$ upper surface

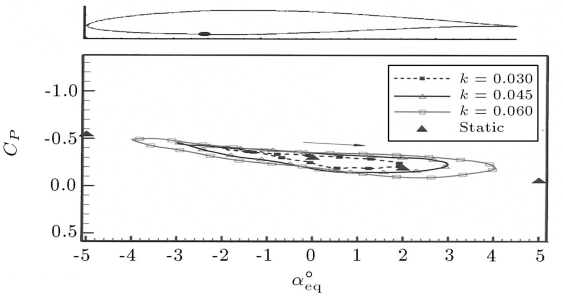

(f) $x/c = 30\%$ lower surface

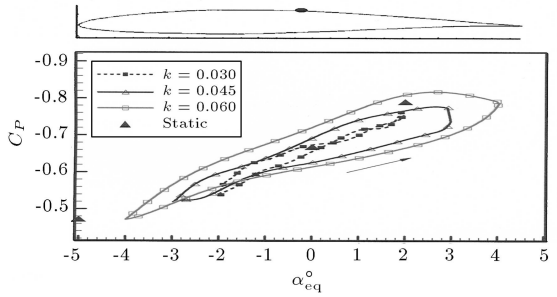

(g) $x/c = 50\%$ upper surface

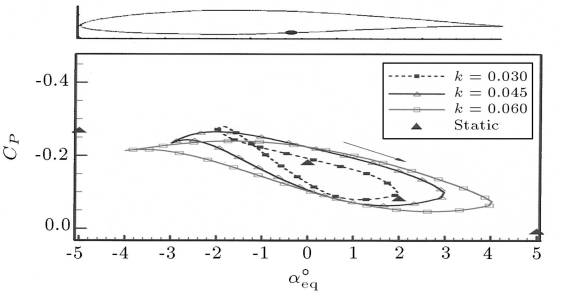

(h) $x/c = 50\%$ lower surface

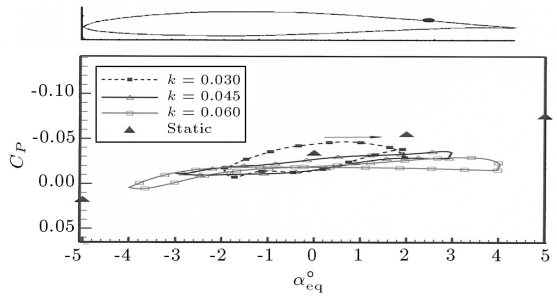

(i) $x/c = 85\%$ upper surface

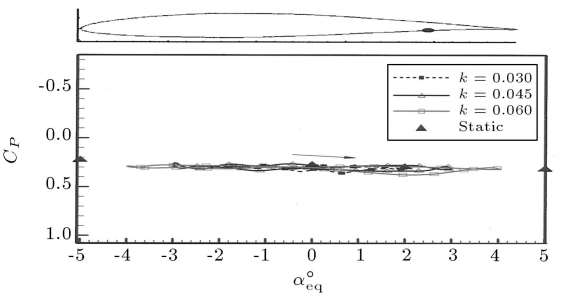

(j) $x/c = 85\%$ lower surface

Figure 5. Variations of the pressure coefficient vs equivalent angle of attack with $\alpha_0 = 0°$.

almost constant for $k = 0.045$ and 0.06. However, for the lowest reduced frequency case, $k = 0.03$, the variations, though small, are more than the other cases (Figure 5i).

By further inspecting Figure 5, it is seen that increasing the reduced frequency increases the induced angle of attack and has a pronounced effect on the surface pressure ports near the leading edge, $x/c < 50\%$, for the upper surface and $x/c < 15\%$ for the lower surface. For these pressure ports, as the reduced frequency is increased from $k = 0.03$ to $k = 0.06$, the hysteresis loop widens a lot. In the rear part of the airfoil, however, there is no difference between the values of the C_P during upstroke and downstroke motions and also the loops become horizontal (Figures 5i and 5j). This indicates that plunging the model has no significant effect on the rear part of the airfoil. Further, from this figure, note that the maximum dynamic pressure coefficient, $|C_P|$, occurs at a maximum induced angle of attack for all three reduced frequencies and the location of the maximum suction is near the $x/c = 30\%$ port on the suction side of the airfoil (Figure 5e).

In Figure 6, the model was set to an incident of 10°, which is near the static stall angle of attack for this airfoil, $\alpha_{\text{stall,,static}} \approx 10°$. For the pressure port located at $x/c = 2\%$ of the upper surface, it is seen that, for the higher reduced frequency case, $k = 0.06$, the pressure hysteresis loop has a counterclockwise direction, but for the other two lower reduced frequency cases, $k = 0.03$ and $k = 0.045$, the "figure eight" shape is evident, which indicates that the flow has a lead-lag effect for this port at these reduced frequencies. The loops aren't wide and both static and dynamic data are almost identical (Figure 6a). For the pressure port located at $x/c = 15\%$ of the upper surface (Figure 6c) and for the reduced frequency of 0.06, the "figure eight" shape is seen in the hysteresis loop, which indicates that the loop changes direction from counterclockwise to clockwise, but the other two reduced frequency cases have clockwise directions. The direction of the loops remains clockwise for all three reduced frequency cases for all pressure ports. For the lower surface pressure ports, all of the hysteresis loops are clockwise and are changed into a nearly straight line, coinciding with their corresponding static data (Figuresd 6b-6j). From this figure, it is seen that maximum dynamic suction occurs at the locations near the leading edge, $x/c = 2\%$, of the upper surface. Further, it is noted that increasing the reduced frequency at angles around the static stall angle of attack of the airfoil has strange effects on its pressure distribution. As indicated in Figures 6a and 6c, the equivalent angle of attack for the maximum $|C_P|$ increases as the reduced frequency is increased, i.e. from $\alpha_{\text{eq}} = 11°$ at $k = 0.03$ to $\alpha_{\text{eq}} = 13°$ at $k = 0.06$ (Figure 6c). Two viscous flow effects play a significant role in the variations of pressure distribution in this region. One is the integrated effect of the time-lagged external pressure gradient on the boundary layer development. The other is the so-called "leading-edge jet" effect. As the airfoil leading edge moves upward (with respect to the equivalent angle of attack), the boundary layer between the stagnation and separation points experiences a moving wall/wall jet effect, very similar to that observed on a rotating cylinder. Thus, the dynamic boundary layer has a fuller profile than the steady case and, therefore, further resists the adverse pressure gradient, hence, delaying separation phenomenon. On the down stroke, the effect is opposite, separation is promoted. There is an additional viscous flow effect of the spilled leading-edge vortex at larger amplitudes and higher frequencies [4].

Figure 7 shows variations of the pressure coefficient, with the equivalent angle of attack for the mean angle of attack of 18°, which is above the static stall angle of attack, $\alpha_{\text{mean}} > \alpha_{\text{stall,static}}$. It is seen that, for the pressure port located at $x/c = 2\%$ of the upper surface (Figure 7a), for all three reduced frequencies tested, the "figure eight" shape is evident, which shows the change of direction from clockwise to counterclockwise. The crossover points are around 19-20 degree angles of attack. For other upper surface pressure ports, however, the hysteresis loops for all three reduced frequencies are clockwise. The same trend is seen for the lower surface pressure ports, too. The only difference is that, for the lower surface pressure ports, the loops become almost horizontal.

By inspecting Figure 7, it is clearly seen that the maximum suction is close to the leading edge, $x/c = 2\%$ (Figure 7a). In this location, the maximum dynamic $|C_P|$ occurs at a maximum induced angle of attack and the mean slope of the hysteresis loop is relatively high. However, for the next two pressure ports, $x/c = 15\%$ and 30%, the maximum dynamic $|C_P|$ occurs at the minimum induced angle of attack (Figures 7c and 7e). The effect of the reduced frequency is, not only to induce higher amplitude of the angle of attack, but also to increase the width of the hysteresis loops, especially at pressure port locations between $x/c = 15\%$ and $x/c = 50\%$ of the upper surface. This means that, by increasing the reduced frequency, the differences between dynamic C_P's in the upstroke portion of the loop and downstroke portion for these pressure ports, $x/c = 15$ and 30%, become larger. This phenomenon could be caused by the separated flow over a large portion of the airfoil prior to the oscillation, since $\alpha_{\text{mean}} > \alpha_{\text{stall,,static}}$. Thus, during the upstroke motion, a leading edge vortex sheds downstream and, in the downstroke motion, this vortex does not fully reattach, creating a wide hysteresis loop. For the pressure port located at $x/c = 2\%$ (Figure 7a), the vortex sheds, but never reattaches.

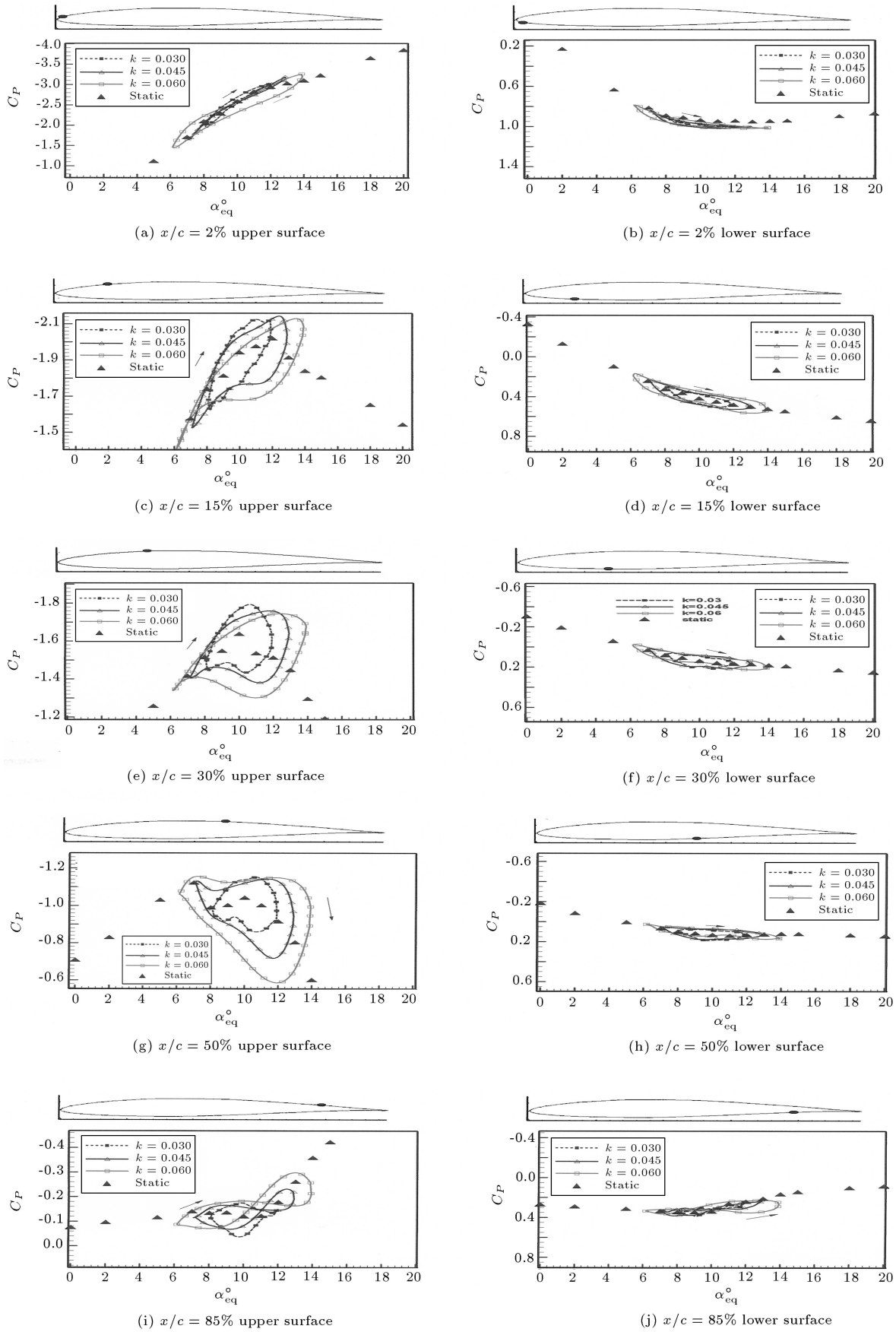

(a) $x/c = 2\%$ upper surface

(b) $x/c = 2\%$ lower surface

(c) $x/c = 15\%$ upper surface

(d) $x/c = 15\%$ lower surface

(e) $x/c = 30\%$ upper surface

(f) $x/c = 30\%$ lower surface

(g) $x/c = 50\%$ upper surface

(h) $x/c = 50\%$ lower surface

(i) $x/c = 85\%$ upper surface

(j) $x/c = 85\%$ lower surface

Figure 6. Variations of the pressure coefficient vs equivalent angle of attack with $\alpha_0 = 10°$.

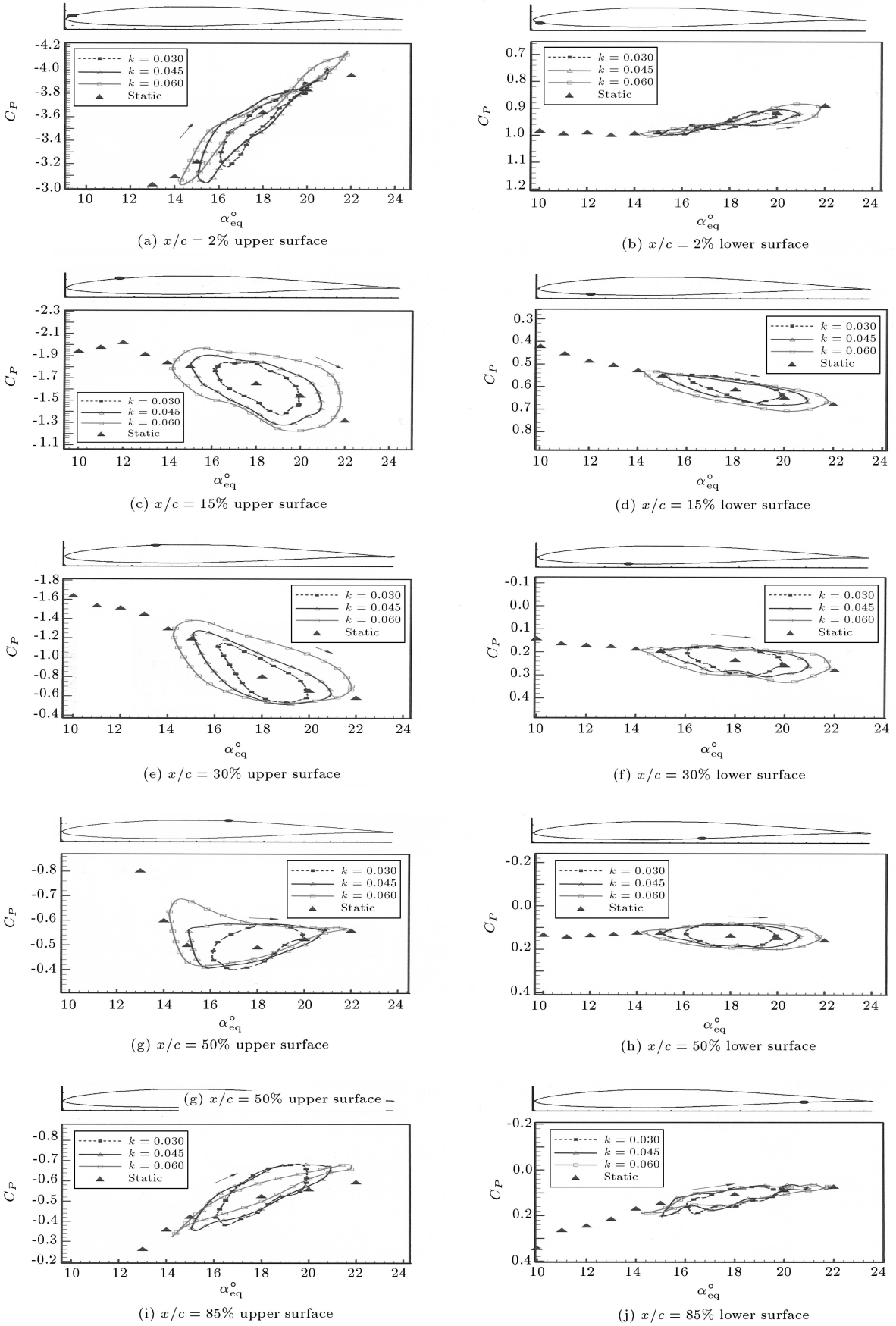

(a) $x/c = 2\%$ upper surface

(b) $x/c = 2\%$ lower surface

(c) $x/c = 15\%$ upper surface

(d) $x/c = 15\%$ lower surface

(e) $x/c = 30\%$ upper surface

(f) $x/c = 30\%$ lower surface

(g) $x/c = 50\%$ upper surface

(h) $x/c = 50\%$ lower surface

(i) $x/c = 85\%$ upper surface

(j) $x/c = 85\%$ lower surface

Figure 7. Variations of the pressure coefficient vs equivalent angle of attack with $\alpha_0 = 18°$.

Figure 8 shows variations of the dynamic pressure coefficient with dimensionless time for eight upper surface pressure ports from the leading edge to the trailing edge, and for two different reduced frequencies, $k = 0.03$ and 0.06. For this case, the model was set to an angle of attack of 10 degrees and plunged at an amplitude of ±15 cm. On the top of Figure 8, variations of the corresponding equivalent angles of attack with time are shown. Note that the amplitude of the induced angle of attack for $k = 0.03$ is about 2 degrees (Figure 8a), however, for $k = 0.06$, it is doubled and is equal to 4 degrees (Figure 8b).

By inspecting Figure 8a, it is seen that, for pressure ports located at $x/c < 15\%$, the flow nearly follows the model motion and the resultant equivalent angle of attack and C_P data varies in a type of cosine form. The magnitude of C_P for all of the aforementioned ports decreases sharply, reaching minimum value at $\tau \approx 0.45$. However, the absolute value of C_P varies between each other, i.e., $|C_{P\max}|$ for the pressure port located at $x/c = 0.5\%$ is the highest. For pressure ports located at $x/c > 15\%$, it is seen that the flow does not follow the model motion and $|C_P|$ remains almost constant during the entire cycle. It means that the oscillation has no effect on the rear portion of the airfoil. For this airfoil, the static stall angle of attack is about 10 degrees, while the data shown in Figure 8 are for $\alpha_0 = 10°$ and oscillated at this angle of attack; hence, the flow over the pressure ports, located at $x/c > 15\%$, was apparently separated.

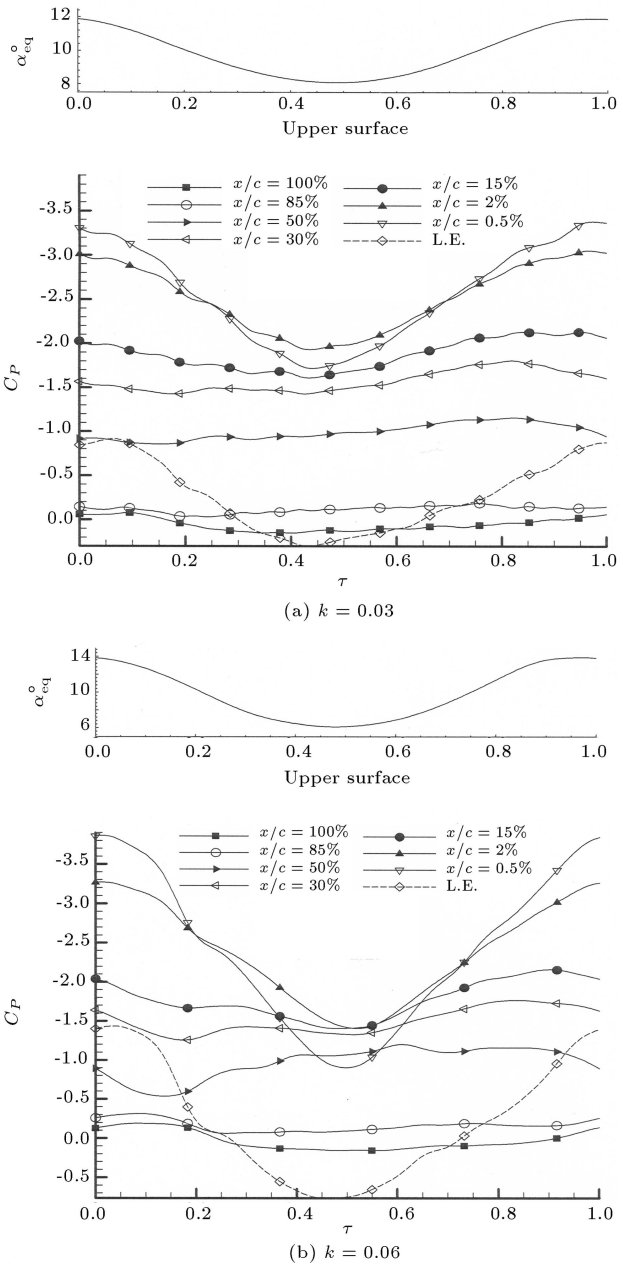

Figure 8. Variations of the pressure coefficient vs dimensionless time with $\alpha_0 = 10°$.

For the higher reduced frequency case, $k = 0.06$, Figure 8b shows that, for all pressure ports located at $x/c > 15\%$, the variations are similar to those of the lower reduced frequency, however, the $|C_P|$ for pressure ports located at $x/c < 15\%$, are higher than those of Figure 8a. By inspecting Figure 8b, it is clearly seen that, for the pressure ports located at the leading edge, $x/c = 0.5\%$ and at $x/c = 2\%$, the magnitude of C_P is nearly constant, or decreases gradually for $0 < \tau < 0.1$ and then starts to decrease sharply by further decreasing the equivalent angle of attack. It seems that the situation is different from the case of $k = 0.03$. On the other hand, as seen, the maximum equivalent angle of attack is at $\tau = 0$, but $|C_{P\max}|$ does not occur at this time. For $k = 0.03$, it occurs at $\tau \approx 0.03$, while, for $k = 0.06$, $|C_{P\max}|$ occurs at $\tau \approx 0.08$. This is due to the effect of reduced frequency on the pressure-gradient-lag. This difference is also seen in Figure 6; for the pressure port located at $x/c = 2\%$, the direction of the hysteresis loops was different for cases where $k = 0.06$ and $k = 0.03$. It means that, due to oscillation, the pressure distribution of the airfoil has some lags, with respect to the change of angle of attack. When the reduced frequency is higher, the model oscillates with higher frequency and so the lags between the equivalent angle of attack and the pressure distribution become larger.

To better understand the pressure variation phenomena over the model, a "carpet-like" graph of C_P is shown in Figure 9. In this figure, all pressure distribution over the airfoil surface, both upper and lower surfaces, during one oscillation cycle, is shown. The comparison is made to investigate the effect of reduced frequency on the surface pressure distribution, when oscillating at different mean angles of attack and reduced frequencies.

By comparing Figures 9a and 9b, it is evident that the effect of reduced frequency is to increase the upper surface suction of the airfoil and results in drastic

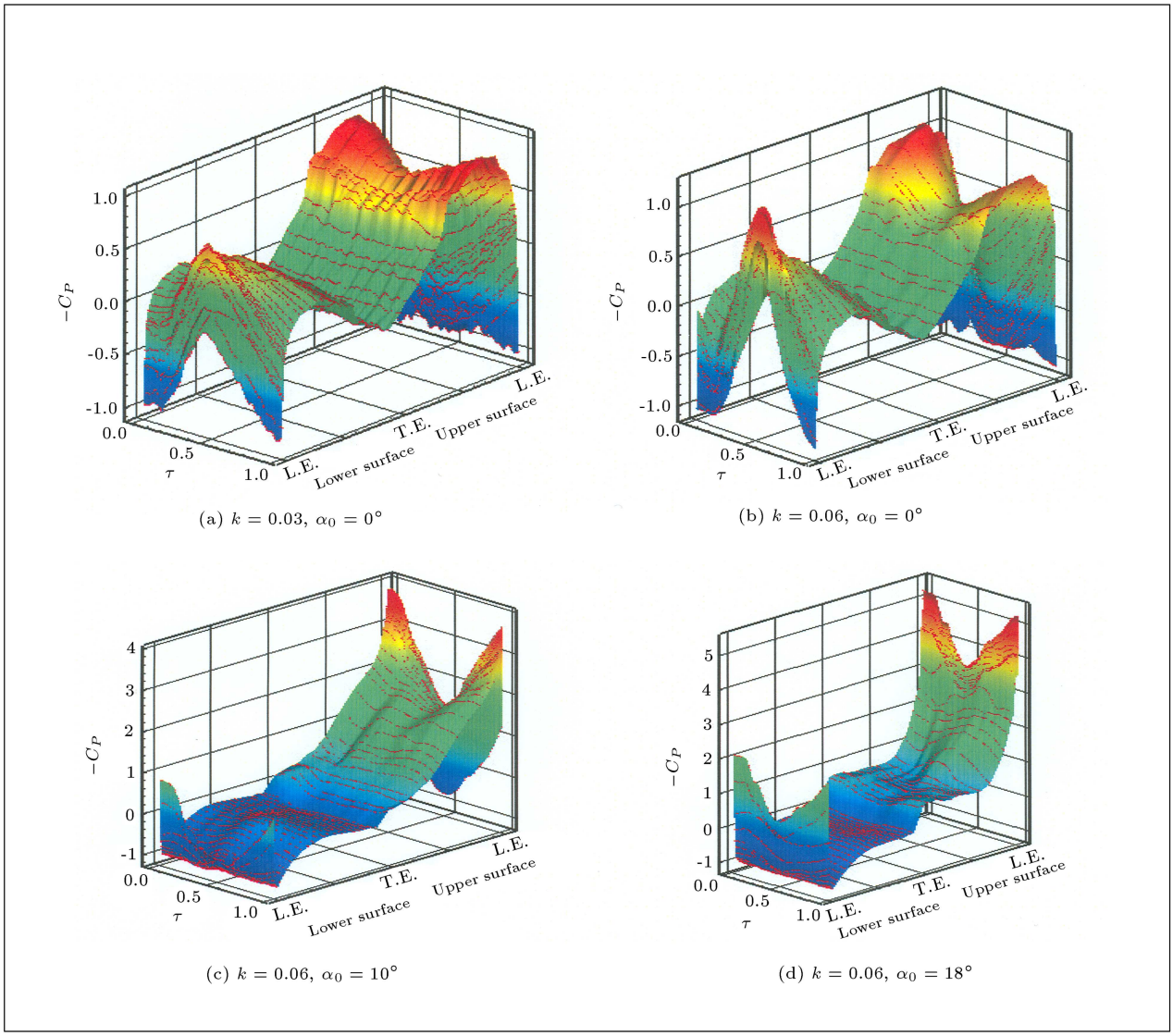

Figure 9. Effect of reduced frequency and incident angle on pressure distribution.

variations of $|C_P|$ during one oscillation cycle. As seen, when oscillating the airfoil at zero mean angle, all pressure ports located near the leading edge (both upper and lower surfaces) show strong suction during the mid oscillation cycle, $\tau \approx 0.5$. The magnitude of $|C_P|$ at this location increases strongly as the reduced frequency increases. This phenomenon is probably due to the cambering effect and is seen only for zero mean angle of attack.

By inspecting Figures 9b to 9d, it is seen that, when oscillating the airfoil at higher mean angles, the maximum suction, $|C_{P\max}|$, increases and its location moves toward the leading edge. It is seen from Figure 9b that $|C_{P\max}|$ is about 1 and its location is near $x/c = 15\%$. For $\alpha_0 = 10°$, $|C_{P\max}| \approx 4$ and occurs at the pressure port located at about $x/c = 0.5\%$ (Figure 9c). For $\alpha_0 = 18°$, $|C_{P\max}| \approx 5$ (Figure 9d) and its location is very close to the leading edge. Also, it is evident that $|C_P|$ drops sharply after the suction peak, which is an indication of the presence of the dynamic vortex shedding from the leading edge of the airfoil.

Unsteady Aerodynamic Loads

The unsteady aerodynamic loads were calculated from the surface pressure measurements, 64 ports, along the chord, for both upper and lower surfaces of the model. The individual, C_l, C_d and C_m, hysteresis loops are shown in Figures 10 to 12, respectively. The unsteady aerodynamic loads are shown for three different mean angles of attack of 0, 10 and 18 degrees and for reduced frequencies of 0.03, 0.045 and 0.06 for constant plunging amplitude of ±15 cm. An arrow gives the

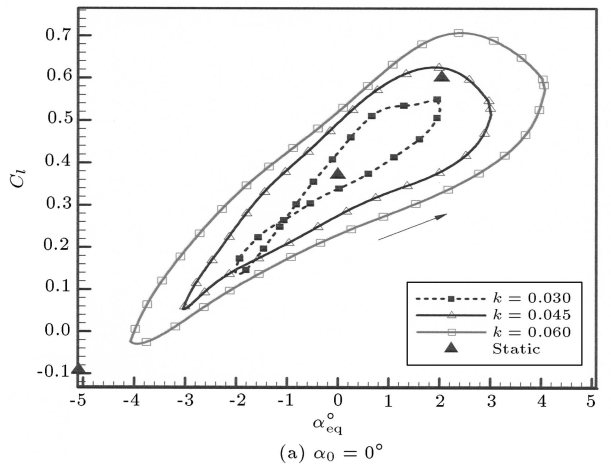

(a) $\alpha_0 = 0°$

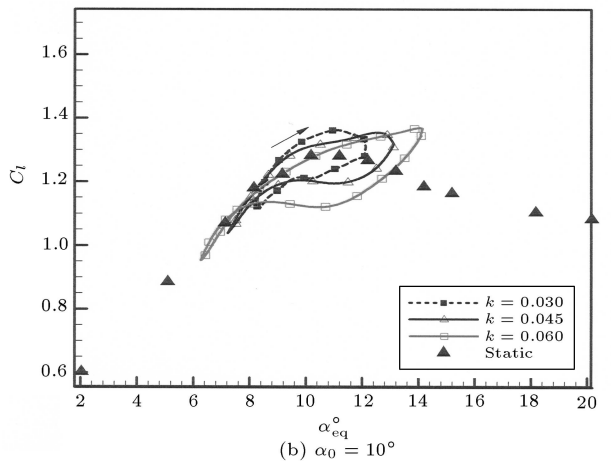

(b) $\alpha_0 = 10°$

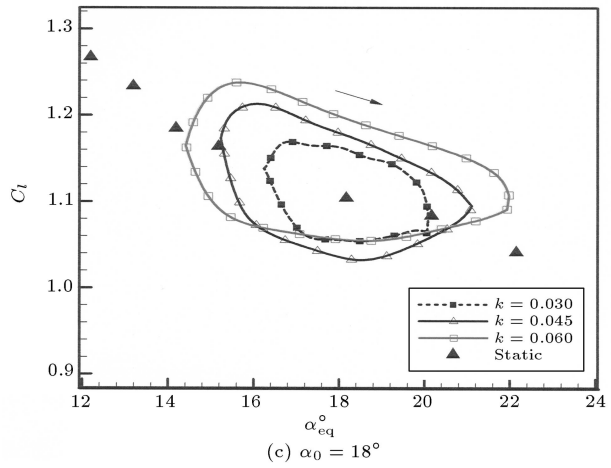

(c) $\alpha_0 = 18°$

Figure 10. Variations of the lift coefficient vs equivalent angle of attack.

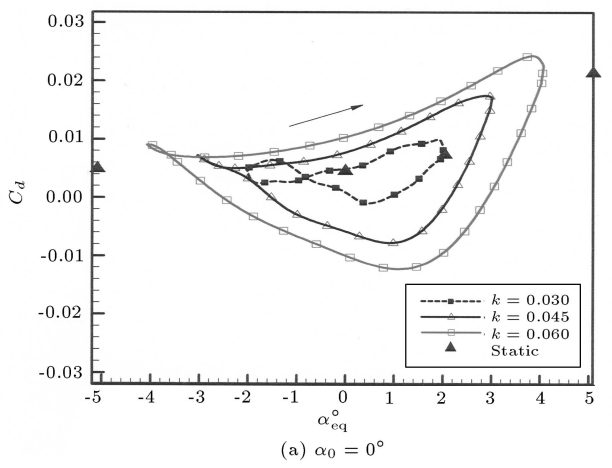

(a) $\alpha_0 = 0°$

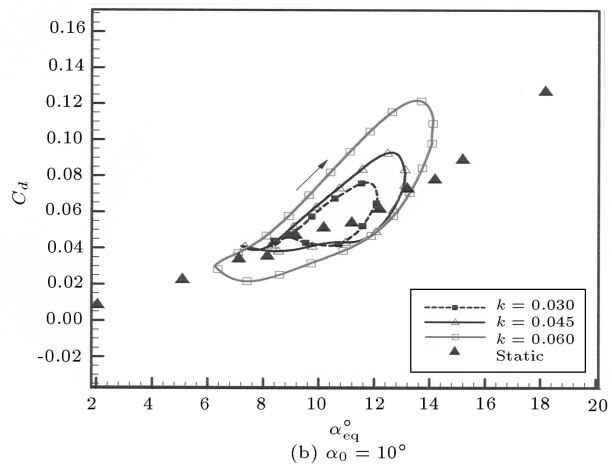

(b) $\alpha_0 = 10°$

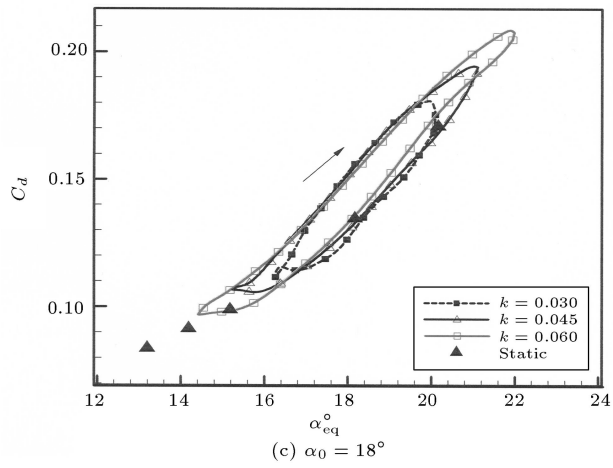

(c) $\alpha_0 = 18°$

Figure 11. Variations of the pressure drag coefficient vs equivalent angle of attack.

direction of each loop. The corresponding static values are shown for comparison.

Figure 10 shows variations of C_l with the equivalent angle of attack for three different mean angles of attack. In the linear part of the static C_l values (Figure 10a), the slopes of the hysteresis loops tend to follow the steady data. The directions of the hysteresis loops are counterclockwise for higher reduced frequency cases, $k = 0.045$ and 0.06, which means the lift in the upstroke curve lags the static data, while, in the down stroke portion, it leads the corresponding static values. For the lower reduced frequency, $k = 0.03$, however,

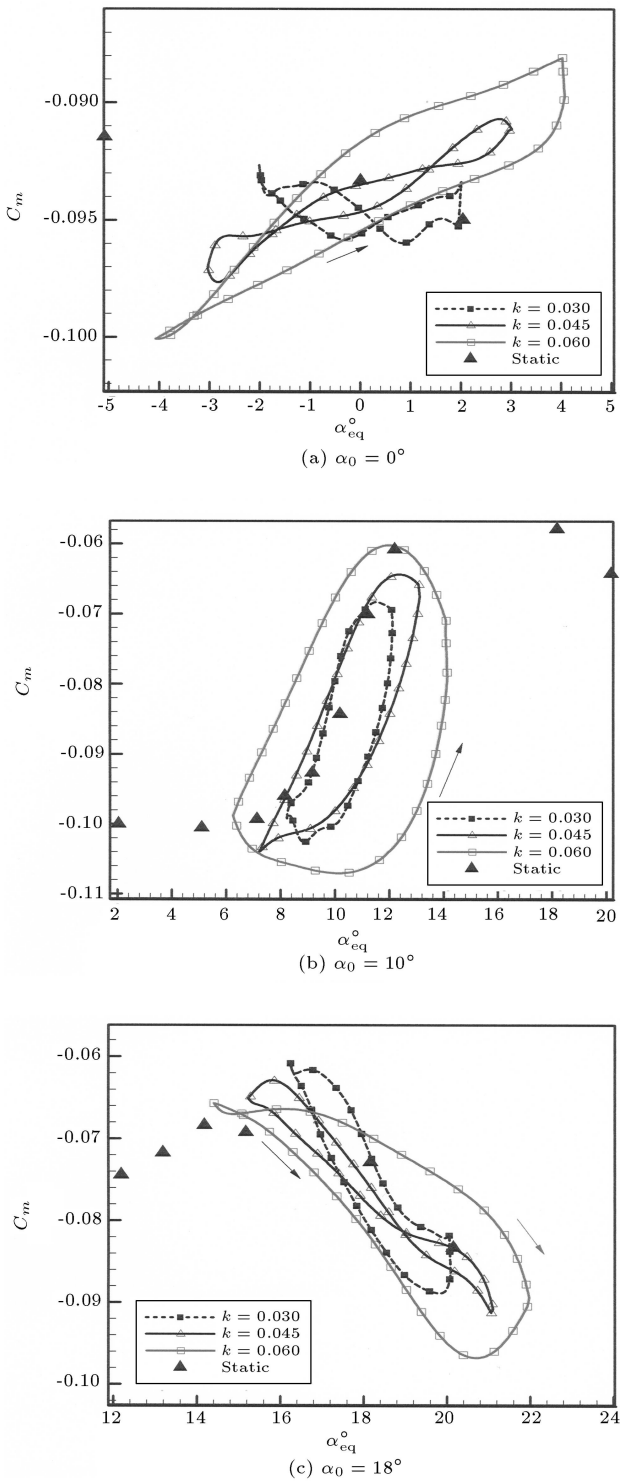

Figure 12. Variations of the pitching moment coefficient vs equivalent angle of attack.

the hysteresis loop shows a "figure eight" shape. This may indicate that there is an undershoot of lift in the upstroke part of the curve at high equivalent angles of attack, while, at the low equivalent alpha, the reverse is true; there is an overshoot. Consequently, there is a crossover point; the upstroke and downstroke lift coefficients are the same for a specific induced angle of attack, $\alpha_{eq} = -1°$. As seen from Figure 10a, the effect of increasing the reduced frequency is to increase the amplitude of the induced alpha, while widening the hysteresis loops. Looking at Figure 10b, it is seen that plunging the airfoil near its static stall angle causes different trends in the dynamic lift coefficients. At a reduced frequency of 0.03, the direction of the loop is clockwise, but at reduced frequencies of 0.045 and 0.06, the direction of the C_l hysteresis loops changes from lag to lead with crossover points near $\alpha_{eq} = 9°$ for $k = 0.045$ and about $\alpha_{eq} = 8°$ for $k = 0.06$. In this region, increasing the reduced frequency induces higher maximum lift value and postpones the stall to a higher equivalent angle of attack. Plunging the airfoil with a mean angle of 18°, or in the post stall region, causes the hysteresis loops of C_l to become clockwise for all three reduced frequencies (Figure 10c). This is due to the influence of different time lags and vortex shedding. As a fact, when oscillating the airfoil with lower mean angles, the direction of the hysteresis loops are strongly affected by the trailing edge wakes and the moving wall effects. However, when oscillating with higher incidence, there exists a separated flow region behind the airfoil, and vortex shedding plays an important role in the trends of the loops.

Figure 11 shows the C_d hysteresis loops. It must be noted that the drag coefficients shown here are only a pressure drag of the airfoil, which is calculated via surface pressure measurements. As the mean angle of attack increases (Figure 11a-c), the average values of C_d also increase. The directions of the hysteresis loops are clockwise for nearly all cases, which mean that the dynamic pressure drag of the airfoil in the upstroke curve is more than that of the down stroke. Also, from Figure 11a, it is seen that for the two higher reduced frequency cases, $k = 0.045$ and 0.06, parts of the dynamic C_d curves show negative values. This means that, for a portion of the oscillation, the airfoil produces thrust force instead of drag, which is due to the different direction of the wake vortices shedding from the trailing edge of the airfoil.

Figure 12 shows variations of the pitching moment coefficient about 1/4 chord of the airfoil with the equivalent angle of attack. The counterclockwise direction of the $C_m - \alpha$ hysteresis loop means positive aerodynamic damping, which produces stability in the oscillating motions [11,12].

In Figure 12a and for $k = 0.06$, the C_m loop is counterclockwise, but for $k = 0.03$ and $k = 0.045$, there exists a "figure eight" shape; i.e. the pitching moment develops into two loops, where the second loop is traversed in a clockwise direction and, thus, represents a negative damping contribution. With further increase in the mean angle of attack (Figure 12b) for all three reduced frequencies, the loops become

counterclockwise. Also, from Figure 12c and for $k = 0.03$, the direction of the C_m loop is counterclockwise, but by increasing the reduced frequency, the reverse is true and the damping during the cycle decreases.

Figure 13 shows variations of the maximum C_l and dynamic stall angle with reduced frequency. As shown in this figure, increasing the reduced frequency postpones the stall to higher angles of attack. Also, a higher value of C_l is induced by plunging the airfoil with larger reduced frequencies. Furthermore, the rate of increase varies with increasing the reduced frequencies. As the reduced frequency increases, the rate of increase of both maximum C_l and dynamic stall angle increases, too.

Figure 14 shows a comparison between the authors test data and the potential flow theory (Theodorsen's theory) [13] for the unstalled case. It is seen that, under the same condition, there is qualitative agreement between the lift coefficient of the potential flow theory and the authors result. Note that Theodorsen's method is for a very thin airfoil, flat plate, while the present airfoil has a thickness ratio of about 16%.

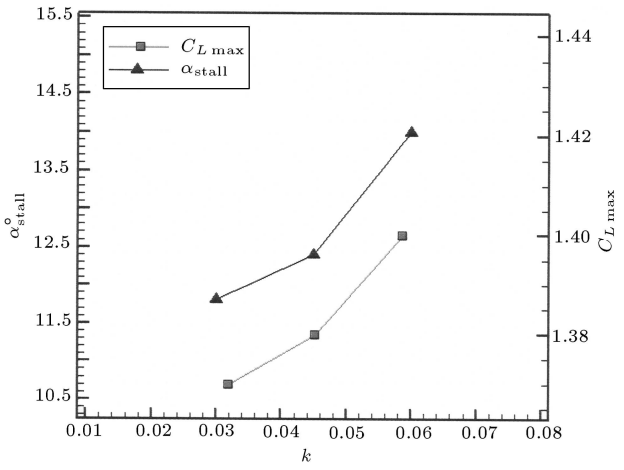

Figure 13. Variations of the $C_{L\,\max}$ and dynamic α_{stall} with reduced frequency.

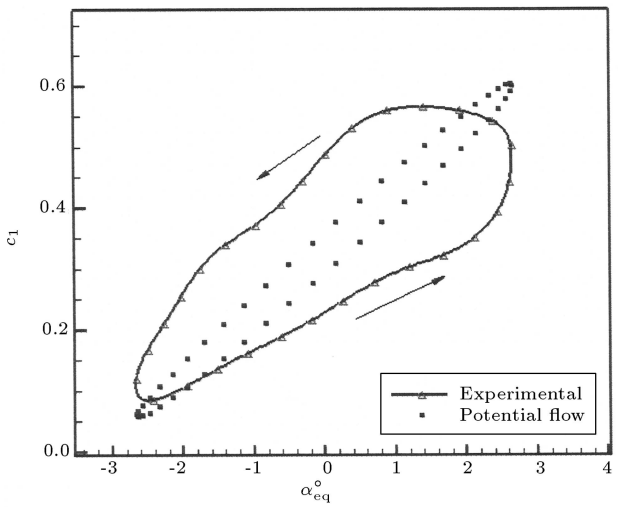

Figure 14. Comparison of the experimental data with the potential flow theory, $\alpha_0 = 0^\circ$ and $k = 0.058$.

CONCLUSION

An extensive experimental investigation was conducted on an oscillating airfoil in a plunge mode over a range of reduced frequencies, $k = 0.03 - 0.06$, from low to high angles of attack. The effect of reduced frequency was to increase the upper surface suction of the airfoil and resulted in large variations of $|C_P|$ during the oscillation cycle. By plunging the airfoil at higher mean angles, the maximum suction of the airfoil increased and its location moved toward the leading edge. The unsteady aerodynamic loads were calculated using surface pressure measurements. Variations of the aerodynamic coefficients with the equivalent angle of attack showed strong sensitivity to the reduced frequency and mean angles of attack. It was concluded that the direction of the lift coefficient hysteresis loops changes from counterclockwise to clockwise with increasing the mean angle of attack. However, all C_d hysteresis loops had the same clockwise directions. Pitching moment coefficients were also sensitive to both reduced frequency and mean angle of attack. The data showed that increasing the mean angle of attack resulted in decreasing damping of the airfoil.

NOMENCLATURE

α	angle of attack (deg)
α_0	mean angle of attack (deg)
h	plunging displacement (cm)
H	amplitude of plunging motion (cm)
$\overline{h}$	dimensionless plunging amplitude, $\overline{h} = \frac{2H}{c}$
$\overline{\alpha}$	amplitude of pitching motion (deg)
k	reduced frequency, $k = \frac{\pi f c}{U_\infty}$
f	plunging frequency (Hz)
U_∞	free stream velocity
c	airfoil chord (m)
τ	dimensionless time, $\tau = t/T$
t	time (sec)
T	period of oscillation
i	$\sqrt{-1}$
C_l	lift force coefficient
C_d	drag force coefficient
C_m	pitching moment coefficient about $c/4$

L.E.	leading edge
T.E.	trailing edge
$()_{eq}$	equivalent motion

REFERENCES

1. Leishman, J., *Principles of Helicopter Aerodynamics*, Cambridge Press (2000).
2. Johansen, J. "Unsteady airfoil flows with application to aero elastic stability", Riso Laboratory, Roskilde, Denmark (Oct. 1999).
3. Carta, F.A. "A comparison of the pitching and plunging response of an oscillating airfoil", *NASA CR-3172* (1979).
4. Ericson, L.E. and Reding, J.P. "Unsteady flow concepts for dynamic stall analysis", *AIAA Journal of Aircraft*, **21**(8), pp. 601-606 (Aug. 1984).
5. Soltani, M.R., Rasi Marzabadi, F. and Seddighi, M. "Surface pressure variation on an airfoil in plunging and pitching motions", *25th ICAS Congress*, Hamburg, Germany, 3-8 September (2006).
6. Tyler, J.C. and Leishman, J.G. "An analysis of pitch and plunge effects on unsteady airfoil behavior", *Presented at the 47th Annual Forum of the American Helicopter Society* (May 1991).
7. Soltani, M.R., Rasi, F., Seddighi, M. and Bakhshalipour, A. "An experimental investigation of time lag in pressure-measuring systems", *AIAC-2005-028, Presented at the 2nd Ankara International Aerospace Conference*, Ankara, Turkey, Aug. 22-25 (2005).
8. Mani, M., Soltani, M.R. and Tolouei, E. "An experimental study for pressure measurements of time lag in different tubes", *Amirkabir Journal of Science and Technology*, **16**(6113), pp. 127-137 (2005).
9. Barlow, J.B., Rae, W.H. and Pope, A., *Low-Speed Wind Tunnel Testing*, John Wiley & Sons, 3rd Edition (1999).
10. Beckewith, T.G., Marangoni, R.D. and Lienhard V.J.H., *Mechanical Measurements*, Addison-Wesley Publishing Company, Fifth Edition (1993).
11. Soltani, M.R., Bakhshalipour, A. and Seddighi, M. "Effect of amplitude and angle of attack on the unsteady surface pressure of a pitching airfoil", *Journal of Aerospace Science and Technology*, **2**(4), pp. 9-27 (2005).
12. Soltani, M.R., Rasi Marzabadi, F. and Bakhshalipour, A. "Investigation of plunging oscillation effects on aerodynamic coefficients of an airfoil", *14th Annual (International) Conference of Mechanical Engineering*, Iranian Society of Mechanical Engineering, May (2006).
13. Theodoresen, T. "General theory of aerodynamic instability and the mechanism of flutter", *NACA TR-496* (1935).